WILEY-VCH

DOI: 10.1002/ ((please add manuscript number))

Article type: Full Paper

Surface passivation for reliable measurement of bulk electronic properties of heterojunction devices

Benjamin Bissig[1], Carlos Guerra-Nunez[2], Romain Carron[1], Shiro Nishiwaki[1], Fabio La Mattina[3], Fabian Pianezzi[1], Paolo A. Losio[4], Enrico Avancini[1], Patrick Reinhard[1], Stefan Haass[1], Martina Lingg[1], Thomas Feurer[1], Ivo Utke[2], Stephan Buecheler[1] and Ayodhya N. Tiwari[1]*

Benjamin Bissig[1], Carlos Guerra-Nunez[2], Dr. Romain Carron[1], Dr. Shiro Nishiwaki[1], Dr. Fabio La Mattina[3], Dr. Fabian Pianezzi[1], Dr. Paolo A. Losio[4], Enrico Avancini[1], Dr. Patrick Reinhard[1], Stefan Haass[1], Martina Lingg[1], Thomas Feurer[1], Dr. Ivo Utke[2], Dr. Stephan Buecheler[1] and Prof. Dr. Ayodhya N. Tiwari[1]

1) Laboratory for Thin Films and Photovoltaics, Empa - Swiss Federal Laboratories for Materials Science and Technology, Ueberlandstrasse 129, 8600 Duebendorf, Switzerland
2) Laboratory for Mechanics of Materials and Nanostructures, Empa - Swiss Federal Laboratories for Materials Science and Technology, Feuerwerkerstrasse 39, 3602 Thun, Switzerland
3) Reliability Science and Technology Laboratory, Empa - Swiss Federal Laboratories for Materials Science and Technology, Ueberlandstrasse 129, 8600 Duebendorf, Switzerland
4) Zurich University of Applied Sciences (ZHAW), School of Engineering, Institute of Computational Physics, Technikumstrasse 9, 8401 Winterthur, Switzerland

E-mail: Stephan.Buecheler@empa.ch

Keywords: CIGS, electron beam induced current (EBIC), surface passivation, atomic layer deposition (ALD)

Quantum efficiency measurements of state of the art Cu(In,Ga)Se_2 thin film solar cells reveal current losses in the near infrared spectral region. These losses can be ascribed to inadequate optical absorption or poor collection of photo-generated charge carriers. Insight on the limiting mechanism is crucial for the development of more efficient devices. The electron beam induced current measurement-technique applied on device cross-sections promises an experimental access to depth resolved information about the charge carrier collection probability. Here, this technique is used to show that charge carrier collection in Cu(In,Ga)Se_2 deposited by multistage co-evaporation at low temperature is efficient over the optically active region and collection losses are minor as compared to the optical ones. Implications on

the favorable absorber design are discussed. Furthermore, we observe that the measurement is strongly affected by cross-section surface recombination and an accurate determination of the collection efficiency is not possible. Therefore we propose and show that the use of an Al_2O_3 layer deposited onto the cleaved cross section significantly improves the accuracy of the measurement by reducing the surface recombination. A model for the passivation mechanism is presented and the passivation concept is extended to other solar cell technologies such as CdTe and Cu2(Zn,Sn)$(S,Se)_4$.

1. Introduction

The quantum efficiency (QE) of heterostructure solar cells is often significantly reduced as compared to theoretical Shockley-Queisser limit, this especially in the near infrared region (NIR).[1] Generally, these losses can be caused by parasitic and incomplete absorption or non-efficient charge carrier collection.[2] The electron beam induced current technique (EBIC) promises a reliable and simple experimental way to estimate collection losses but it tends to be impeded by effects of surface recombination.[3-5]

For CIGS absorbers EBIC has been employed for investigation of collection dependence on Ga content[6], grain boundaries[4,7], buffer layers[8], absorber composition[9], buried junctions[10], bias voltage[11] and voids[12,13]. The typically reported EBIC profile FWHM (for E_B ~ 1-10 keV) lies between 0.5 µm – 1 µm.

For CIGS with compositional grading we will show that conventional EBIC seems to critically underestimate the real collection length and we propose that the application of a conformal Al_2O_3 passivation layer can significantly improve signal magnitude and especially information content. This approach is employed to identify the origin of the current losses in state of the art Cu(In,Ga)Se_2 (CIGS) thin film solar cells for which recently a series of record efficiencies > 20 % was reported.[14-16]

Firstly we will review how surface recombination affects the EBIC measurement, see 1.1. Secondly, results for Al_2O_3 passivated EBIC measurements are presented in 2.1 and 2.2. In 3.1 the appraoch is validated by showing that the device EQE can only be accurately predicted by EBIC measurements that employ a passivation layer. Aspects of the microscopic mechanism of the passivation are discussed in 3.2. In 3.3 the approach is generalized for CdTe and $Cu_2(Zn,Sn)(S,Se)_4$ devices. Finally, implications on future device design are discussed in chapter 4.

1.1. Conditions for accurate determination of charge collection probability by electron beam induced current measurements (EBIC)

EBIC can be used to experimentally access the local *carrier collection function f(z)*, defined as the probability for locally generated electron to be collected and measured as device current. **Figure 1** illustrates the measurement principle, performed under short circuit conditions. The high electron energy (E_B) leads to e-h pair generation in the semiconductor (bandgap E_G) and the injected beam current I_{INJ} is gained by a factor on the order of E_B/E_G resulting in induced currents I_{BIC} in the 1-10 nA range for typical parameters E_B = 5 keV and I_{INJ} = 20 pA. EBIC conventionally denotes the mapping of the current I_{BIC} over a region of interest e.g. across the cross section of the device, see Figure 1 c). The secondary electron signal is recorded simultaneously, see Figure 1 b).

The measured current I_{BIC} for electron generation at position $\vec{x}$ can be written as the convolution

$$I_{BIC}(\vec{x}) = \int dV\, g(E_B, \vec{x}, \vec{x}')\, f(\vec{x}')\, r(\vec{x}') dV' \quad (1)$$

of the energy dependent carrier generation distribution $g(E_B, \vec{x}, \vec{x}')$ and the collection function $f(\vec{x}')$.[17] The phenomenological term $r(\vec{x}')$ introduced here accounts for recombination due to the presence of the cross section surface and approaches unity deep in the absorber. In order

to measure an EBIC signal which is representative for the collection function *f(x),* following requirements have to be fulfilled:

i) *Low injection energy*: As the generation volume $g(E_B, \vec{x})$ limits the spatial resolution[6,18], low beam energies are required for high resolution sampling of $f(\vec{x}')$. This was also exploited for depth resolved EBIC measurements.[19,20] The typical extend of the generation volume can be estimated according to the expression

$$R = \frac{0.043}{\rho} \frac{\mu m\, g}{cm^3} \left(\frac{E_B}{1\ keV}\right)^{1.75} \quad (2)$$

where ρ denotes the host material density.[21] Assuming ρ = 5.7g cm^{-3}, **Equation 2** suggests a measurement resolution of ~ 120 nm at 5 keV. We estimate similar generation ranges by CASINO[22] simulations and further it was found that for E_B >1 keV the addition of a ~ 6 nm surface oxide on the cross section does not significantly affect the electron trajectories in the absorber below, see **Figure S1**.

ii) *Low injection current*: In order to measure the collection function $f(\vec{x})$ which is representative for operation under 1 sun (AM 1.5G spectrum) a low excitation level has to be assured. [18] Therefore, beam currents of 20 pA were used which was found to be significantly below the onset of high injection effects, see **Figure S2**.

iii) *Low cross section surface recombination*: If surface related recombination is effective $(r(\vec{x}) \to 0)$ over the range of electron injection $(g(E_B, \vec{x}) > 0)$ it can reduce the EBIC measurement accuracy. This holds especially in the case of low injection energies with generation in the vicinity of the defect rich surface. Measurements in the limit of high surface recombination have been exploited to estimate cross section and grain boundary surface recombination velocities which were found to be on the order of 10^5 cm s^{-1} and 10^4 cm s^{-1},

respectively. [4] In this cases reliable and direct extraction of the collection function is complicated and fitting procedures are necessary.[3-5] The use of thin amorphous ALD Al_2O_3 layers on the cross section is an attempt to actively reduce the cross section surface recombination for measurements with low injection energy and current which are susceptible for surface recombination. This passivation concept has been recently applied to CIGS solar cells and it was shown that with structured Al_2O_3 layers at the interface between the absorber and the Mo back contact the open circuit voltage V_{OC} of ultrathin (<600 nm) devices can be improved.[23-25]

Finally, the device shunt resistance R_P and amplifier input impedance R_{amp} form a current divider, see Figure 1, that intrinsically complicates the direct comparison of different devices and which makes comparison of EBIC measurements qualitative.

2. Results

EBIC measurements were performed on CIGS reference samples, samples with Cr and Ni impurities and CdTe and Kesterite devices. In the CIGS case, the impurities were introduced from the back contact and cause significantly decreased photocurrents due to introduction of deep recombination centers as reported earlier.[26] **Table 1** compiles photovoltaic parameters of all the samples presented. The CIGS absorber layers were grown by a low temperature multi stage co-evaporation process.

The alumina layers were deposited on the cross-section of freshly cleaved CIGS devices by thermal ALD at 220 °C using Trimethyl-Aluminum (TMA) and H_2O as precursors. It can be expected that amorphous Al_2O_3 layers are formed at the selected deposition temperature, as

such are observed even on single crystalline substrates.[27,28] Air exposure before ALD deposition was on the order of few minutes.

These samples and corresponding reference samples without Al_2O_3 were contacted and EBIC measurements were performed within few hours after mounting. Details on absorber and Al_2O_3 deposition and EBIC acquisition can be found in the experimental section.

2.1. Effects of Al_2O_3 coating on EBIC measurements

Figure 2 shows SE micrographs overlaid with EBIC color maps of representative device cross sections. Beam energy for these measurements was set to 5 keV for high resolution imaging. EBIC maps were normalized and lower signal cutoff was chosen just above background level. The left hand side shows samples without alumina whereas the right hand side shows such with 6 nm Al_2O_3 coating. The uncoated cases all show similar profile full width half maximum (FWHM) around 400 nm and the peak is localized close to the CdS/CIGS interface. Locally, especially in Figure 2 c) the signal extends somewhat deeper into the absorber in the uncoated case. Such local variations of EBIC signal width were found also on Ga ion polished cross sections and showed some dependence on local grain orientations as obtained from electron back scattered detection (EBSD).[4] It seems likely that grain orientation and thus injection probability as well as surface termination (e.g. surface charge and defects) can lead to non-homogenous EBIC profiles.

For the Al_2O_3 coated cases the signal extends more homogenously towards the back contact. For the reference case the collection decreases only very close to the back contact i.e. remains >75% up to 1.6 µm from the CdS/CIGS interface. The FWHM for the reference sample is 1.8 µm and decreases to 1.5 µm and 0.7 µm for the samples with Cr and Ni impurity, respectively. Notably this trend is in qualitative agreement with the device J_{SC} as presented in Table 1. Details on the accuracy of these measurements will be discussed later.

In order to rule out collection improvement due to bulk annealing during the ALD process, a reference sample was annealed under similar conditions as for the Al_2O_3 cases (1h, 220°C, air) but no effect on the EBIC signal was observed (see **Figure S3**). Another reference sample was coated with only 3 nm of Al_2O_3 showing a similar effect as the 6 nm case, see Figure S3.

2.2 Effect of beam energy with and without Al_2O_3 coating

EBIC profiles are shown in dependence on injection energy E_B for the cases with and without Al_2O_3 in **Figure 3** a). The beam energy was increased from 1 keV to 20 keV. It can be seen that the extracted profile is only weakly dependent on injection energy in the Al_2O_3 case while pronounced signal widening is observed for the case without alumina. For 1 keV a signal could only be recorded on the sample with Al_2O_3. Note that the beam widening in the uncoated case cannot be ascribed to the increasing injected depth only, but is also driven by the increasing generation range towards the junction.

Nevertheless, this is a clear indication that in the Al_2O_3 case the EBIC signal is less affected by surface related recombination. In this case, only for the lowest energy of 1 keV a significant reduction of the signal width is observed. A model for the surface passivation mechanism will be discussed below.

3. Discussion

3.1. Validating the approach

In order to evaluate the predictive power of Al_2O_3 enhanced EBIC, the expected EQE was calculated and compared to direct measurements. **Figure 4** a) shows normalized EBIC profiles for the reference sample with and without Al_2O_3 coated cross section, see Figure 2 a) and b). The profiles were calculated from horizontal averages over representative region of 4

µm along the cross section indicated by the dashed squares in Figure 2. For the following numerical calculation, the EBIC profiles were approximated by the dashed lines in Figure 4. To account for the finite excitation range, the approximated profiles were quenched by ~ 100 nm as compared to the raw measurement, giving a rough approximation for the deconvolution of Equation 1.

The interconnection between EQE and EBIC is based on the convolution of collection- $f(x)$ and charge generation function $g(x,\lambda)$ i.e. the external quantum efficiency can be approximated by

$$EQE(\lambda) \propto T(\lambda) \int_0^t f(x) g(x,\lambda) dx, \qquad (3)$$

where t denotes the absorber thickness and λ the photon wavelength. Optical losses due to parasitic absorption and reflection are included by multiplication of the simulated incoherent transmission $T(\lambda)$ through a ZnO:Al/iZnO/CdS/CIGS (CGI and GGI values as measured at the interface and extinction coefficient set $k = 0$) based on reported complex refractive indexes.[29,30] The calculation of $g(x,\lambda)$ is presented in **S4**. Local absorption coefficients $\alpha(x,\lambda)$ were considered in order to account for the influence of compositional variation throughout the absorber. Therefore, *GGI* and *CGI* profiles were measured by secondary ion mass spectroscopy (SIMS)[26] and rescaled by integral compositional ratios as obtained from XRF measurements, see Table 1. The local $\alpha = \alpha(GGI,CGI,E)$ were then derived from transmission and reflection measurements on 10 in-house grown ~ 2 µm thick single stage absorbers detached from the initial Mo substrate, spanning the range $0.15 < GGI < 0.4$ and $0.8 < CGI \leq 1$. These coefficients are considered reliable in the range of $\alpha = 1000\ cm^{-1}$ to $\alpha = 15'000\ cm^{-1}$ with the upper limit defined by the dynamic range of the photospectrometer and the lower limit by interference fringes. To nevertheless include the higher energy range we merged our

model to the one reported by Minoura et al.[30] Details on the procedure are shown elsewhere.[31]

Figure 4 b) shows the EQEs calculated after **Equation 3** for the two cases together with the measured EQE. The EQE calculated from EBIC measurement match the measured EQE only if the EBIC was performed on Al_2O_3 coated cross sections. In contrast, the EQE calculated from the profile belonging to the reference without Al_2O_3 strongly underestimates the measured EQE. The calculation based on Al_2O_3 enhanced EBIC tends to slightly underestimate the measured EQE in the NIR. However, this still holds if ideal collection is assumed. Therefore we ascribe this difference to either a slight underestimation of the NIR absorption coefficient or to the neglected effects of coherent light propagation. Similar comparison for the cases with Cr and Ni impurities is shown in **Figure S5**. The calculation underestimates the measured EQE somewhat in the NIR but promises good overall predictive power. Further discussion on possible deficiencies of the model can be found in S5.

We discuss two further complementary arguments supporting the accuracy of the measured Al_2O_3-EBIC collection functions. Firstly, a SCAPS[32] model of the Ref and Ni case was used to estimate the bulk collection functions for these two cases, see **Figure S6**. Good agreement between Al_2O_3 enhanced EBIC measurement and simulation was found. Secondly, assuming that the uncoated EBIC measurement was representative for the collection function, the absorption coefficients would have to be increased by more than one order of magnitude to match calculated and measured EQE. These arguments support that Al_2O_3 passivates the cross section without significant introduction of artefacts and thus allows extracting more accurate charge collection functions.

3.2. Towards a model for the passivation mechanism

The results shown so far indicate that ALD Al_2O_3 deposition reduces the effect of cross section surface related recombination. For p-type c-si wafers and InGaAs it was proposed that fixed negative charge in the oxide can lead to band bending and therefore reduced effective surface recombination velocities.[33,34] Microscopically, the oxide charge was ascribed to dangling oxygen bonds that cause deep lying acceptor states. When brought into contact to the p-type semiconductor the states become negatively charged and cause surface upward band bending.[34] Oxygen rich Al_2O_3, as detected by XPS within the first 3 nm from the substrate/oxide interface, was suggested to be the origin of the high density of dangling bonds. [34] Similar upward band bending was suggested for the Al_2O_3/CIGS interface to explain increased photoluminescence yield and shifted capacitance-voltage curves.[35-37]

Figure 5 compiles schematics and SCAPS[32] simulation of a model that is suggested to explain the improvement in EBIC accuracy upon Al_2O_3 deposition. It is based on the microscopic surface charge related model introduced above. Figure 5 a) shows the basic model configuration consisting of a CIGS absorber bulk, a defect rich cross section surface/interface (IF) with recombination velocity of $S = 10^5$ cm s^{-1}, and a wide gap insulator with either donor or acceptor states close to the conduction or valence band respectively. The donor/acceptor concentration (the surface or oxide charge) determine the surface band bending. Here, for illustration the fixed surface/oxide charge was set to Q = +/- 5x10^{11} cm^2. This results in a band bending towards the cross section surface of Φ = -510 mV /+10 mV as sketched in Figure 5 b). For simplicity we leave the interface recombination velocity unchanged, but remark that based on DFT calculations also a reduction of the interface defect density by 35% was predicted upon Al_2O_3 deposition.[36]

Next, EBIC electron injection was mimicked by imposing carrier generation at the p-type surface (dashed blue in Figure 5 a) and b)). The generation was set as Gaussian decay towards the bulk with 50 nm characteristic length. This shape does not reflect the real electron scattering, but it was found that details of generation range are not significant for the following discussion as long as generation remains confined to the space charge zone. The generation density was set to remain in low excitation conditions. The model parameters can be found in **Table S7**.

Figure 5 c) shows the steady state *Shockley-Read-Hall (SRH) recombination rate profiles* across the absorber bulk, the space charge region (SCR) and the interface for different cases

i) Φ = 510 mV, downward bending; Recombination rates in the depletion region and at the surface are high. Net bulk recombination rates are very low.

ii) Φ = - 10 mV, upward bending; Space charge region- and surface recombination are reduced. Comparably high bulk recombination rates.

iii) $\Phi \sim 0$ mV, flat bands, no IF recombination; Similar bulk recombination level as in the upward bend case, no surface recombination.

iv) $\Phi \sim 0$ mV, flat bands, IF recombination; Similar to case iii) somewhat reduced bulk but increased surface recombination rates.

Figure 5 d) shows the corresponding *steady state electron densities* across the spatial dimension. Again we discriminate the cases:

i) Φ = 510 mV, downward bending; High electron density towards the surface, near equilibrium electron density in the absorber bulk.

ii) Φ = - 10 mV, upward bending; Reduced surface electron density, that decays towards the bulk with decay length given by the minority carrier diffusion length.

iii) $\Phi \sim 0$ mV, flat bands, no IF recombination; Similar distribution as in the upward bend case is observed except for lack of surface electron depletion.

iv) $\Phi \sim 0$ mV, flat bands, IF recombination; Similar to case iii) but reduced bulk electron density.

In the uncoated case one can expect the bands to be downward bend towards the cross section, see Figure 5b). This was attributed to metal terminated grain boundaries and film surfaces.[38-40] The simulations show high local recombination rates for injection into the depleted/inverted region. This in turn leads to low electron density deeper in the bulk. We propose that this low bulk electron density reflects in the strongly reduced EBIC current for the uncoated case. Note that this mechanism reduces the bulk electron density by one order of magnitude for band bendings as low as Φ = + 25 mV (i.e. only $3x10^{10}$ cm^{-2} positive surface charge).

For the passivated case, the simulations show that the bulk electron density is very close to the case without bend bending and defect free surface (undisturbed bulk case). This explains, how negative surface charge reduces the impact of surface recombination during the EBIC measurement.

The dashed lines in Figure 5 c) and d) show SRH recombination rates and electron densities for electron injection localized 0.5 µm below the surface for Φ = + 510 mV. The bulk electron density then approximates its value in the flatband case without IF defects. This shows, that in case of carrier generation outside the SCR both positive and negative surface charge do passivate the defect rich surface. This bridges our model to the conventional passivation model of weakly absorbing c-Si.[41]

3.3. Extension to other thin films solar cell absorber technologies

Finally, the concept was applied to CdTe and $Cu_2(Zn,Sn)(S,Se)_4$ (Kesterite) based devices, see Table 1. For details on device processing see the experimental section. **Figure 6** shows SE

and EBIC overlays (normalized and background cut off) for Al_2O_3 coated and uncoated devices. It can be seen that the EBIC signal for the Al_2O_3 cases is more homogeneous and extends further towards the back contact. For the CdTe case the observed > 2 μm collection length in connection with the ungraded bandgap profile can explain the measured, steep NIR EQE cutoff.[42] For the Kesterite the interpretation is more complicated due granular morphology towards the back contact.[43] We do not attempt to perform numerical comparison to EQE measurements here but note that the oxygen dangling bond related model as discussed above is expected to be generally applicable for p-type absorbers for which collection efficiency is limited by bulk recombination.

4. Conclusion and Outlook

We point out that the measured EBIC signal convolutes a variety of non-idealities like finite excitation volume and especially surface recombination. Atomic layer deposition of alumina on the measured cross section is suggested to reduce the impact of the latter and allows extracting more accurate information about the charge collection function at low injection energies and thus high resolution.

Applying the approach, we show that the minority carrier collection probability is > 75% up to 1.6 μm from the CdS/CIGS interface for low temperature co-evaporated state of the art CIGS with typical J_{SC} and EQE. This is likely caused by the field assisted charge collection in bandgap graded material. By comparison to the case of ideal collection, we calculate the residual collection loss to be on the order of 0.2 mA cm^{-2}. The optical NIR EQE losses can then be estimated to be ~ 2 mA cm^{-2}. We conclude that these losses can be targeted by engineering of optical absorber thickness. Experimental verification of this is reported elsewhere.[44]

We did not attempt to extract quantitative values for surface recombination velocities and surface charge as the influence of cross section surface roughness would only allow to obtain effective values. Application of this approach to focused ion beam polished cross sections could allow extracting surface recombination properties of passivation layers reliably, and in consequence could serve as tool for optimization of passivating properties in general. The identification of suitable passivation layers and characterization of the interface to the absorber remains a challenging and most important aspect for introduction of advanced passivation concepts in thin film photovoltaics.

More generally, the use of Al_2O_3 or other passivating oxides in order to reduce surface recombination for characterization purpose opens a generic path for investigation of thin film opto-electrical devices where strong surface recombination effects do conceal the bulk properties which are often of primary interest. In cases of photo- or cathodoluminescence (PL, CL) this effect can be exploited to suppress surface recombination paths, to increased signal levels and to stabilize measurement conditions for surfaces prone to degradation. In the case of thin film absorbers, this is especially interesting as screening lengths of negative surface charge on p-type material is low compared to typical photon and electron penetration depths. Therefore, in contrary to passivation by e.g. CdS, such kind of passivation is expected to have only minor influence on excess carrier kinetics in terms of drift effects and thus facilitating interpretation.

5. Experimental Section

Device fabrication and characterization:

CIGS was co-evaporated from elements in a multi stage process at around 450 °C substrate temperature from elemental sources on SLG/Mo substrates. For the samples with Cr and Ni impurities SLG/Mo/impurity/Mo substrates were used. Devices were finished by chemical

bath deposition of CdS and sputtered intrinsic and Al doped ZnO. Details on the process, IV and SIMS measurements are presented elsewhere for CIGS[26], for CdTe[42] and for $Cu_2(Zn,Sn)(S,Se)_4$[45].

Al_2O_3 by atomic layer deposition:

Devices were cleaved and instantaneously transferred into a home built ALD reactor. Al_2O_3 was deposited at a reactor temperature of 220 °C with an alternating precursor mixture of Trimethyl-Aluminium (TMA 97%, Aldrich) kept at room temperature and DI water kept at 40 °C. One ALD cycle consisted of 1 s of pulsing time with 10 s of exposure followed by 30 s of purging for both precursors. The average growth per cycle at 220 °C was ~1.25 Å/cycle. The deposition of 25 and 50 cycles yielded ~3 nm and ~6 nm of Al_2O_3, respectively.

EBIC sample preparation:

Ni (40 nm)/Al (4 µm) contacts of $3x10^{-2}$ cm^{-2} were evaporated onto the AZO before Al_2O_3 coating. Silver paint and Cu wires were used to contact the device to an electrical bridge that was introduced to reduce mechanical stress on the wiring during EBIC measurement. Before introduction the samples into the microscope IV curves of the samples were acquired to check for shunting.

EBIC acquisition:

A Strata FEI 235 Dual Beam was used as electron source were injection energy was in the range of 1 keV - 20 keV and current was set to ~ 20 pA as measured with a faraday cup located on the sample holder. EBIC current was amplified with a gain of $5x10^7$ V/A at an input impedance of 10 kΩ (SRS SR570). Typical acquisition parameters were: pixel dwelling times of 50 µs, field of view around 10 µm and resolution 512^2 px. SE and EBIC signal were simultaneously recorded with a commercially available system from GATAN.

Supporting Information
Supporting Information is available from the Wiley Online Library or from the author.

Acknowledgements

The authors want to thank Till Coester & Petra Gisler for technical support. The work at Empa was partly supported by the National Research Programme "Energy Turnaround" (NRP 70) of the Swiss National Science Foundation (SNSF), the Swiss National Science Foundation (SNSF, grant number 200021_149453 / 1), the Competence Center of Energy and Mobility (grant number 906 CONNECT PV), and the Swiss Federal Office of Energy (SFOE, grant number SI/501145-01).

Received: ((will be filled in by the editorial staff))
Revised: ((will be filled in by the editorial staff))
Published online: ((will be filled in by the editorial staff))

References

[1] W. Shockley, H. J. Queisser, *J. Appl. Phys.* **1961**, *32*, 510-&.

[2] S. Siebentritt, *Sol. Energy Mater. Sol. Cells* **2011**, *95*, 1471-1476.

[3] J. Rechid, A. Kampmann, R. Reinek-Koch, *Thin Solid Films* **2000**, *361*, 198-202.

[4] M. Nichterwitz, D. Abou-Ras, K. Sakurai, J. Bundesmann, T. Unold, R. Scheer, H. W. Schock, *Thin Solid Films* **2009**, *517*, 2554-2557.

[5] J. Kavalakkatt, D. Abou-Ras, J. Haarstrich, C. Ronning, M. Nichterwitz, R. Caballero, T. Rissom, T. Unold, R. Scheer, H. W. Schock, *J. Appl. Phys.* **2014**, *115*.

[6] R. Kniese, M. Powalla, U. Rau, *Thin Solid Films* **2009**, *517*, 2357-2359.

[7] D. Abou-Ras, J. Dietrich, J. Kavalakkatt, M. Nichterwitz, S. S. Schmidt, C. T. Koch, R. Caballero, J. Klaer, T. Rissom, *Sol. Energy Mater. Sol. Cells* **2011**, *95*, 1452-1462.

[8] W. Witte, D. Hariskos, M. Powalla, *Thin Solid Films* **2011**, *519*, 7549-7552.

[9] S. Ishizuka, A. Yamada, P. J. Fons, H. Shibata, S. Niki, *Appl. Phys. Lett.* **2013**, *103*.

[10] S. Ishizuka, A. Yamada, P. J. Fons, Y. Kamikawa-Shimizu, H. Komaki, H. Shibata, S. Niki, *Appl. Phys. Lett.* **2014**, *104*.

[11] D. Abou-Ras, N. Schafer, N. Baldaz, S. Brunken, C. Boit, *AIP Adv.* **2015**, *5*.

[12] M. Richter, I. Riedel, C. Schubbert, P. Eraerds, J. Parisi, T. Dalibor, J. Palm, *Phys. Status Solidi A* **2015**, *212*, 298-306.

[13] D. Lee, J. Lee, S. Heo, J. B. Park, Y. S. Kim, C. B. Mo, K. Huh, J. Yang, J. Nam, D. Baek, S. Park, B. Kim, D. Kim, Y. Kang, *Appl. Phys. Lett.* **2015**, *106*.

[14] A. Chirila, P. Reinhard, F. Pianezzi, P. Bloesch, A. R. Uhl, C. Fella, L. Kranz, D. Keller, C. Gretener, H. Hagendorfer, D. Jaeger, R. Erni, S. Nishiwaki, S. Buecheler, A. N. Tiwari, *Nat. Mater.* **2013**, *12*, 1107-1111.

[15] P. Jackson, D. Hariskos, R. Wuerz, O. Kiowski, A. Bauer, T. M. Friedlmeier, M. Powalla, *Phys. Status Solidi RRL* **2015**, *9*, 28-31.

[16] Solar Frontier, Solar Frontier Achieves World Record Thin-Film Solar Cell Efficiency: 22.3%, http://www.solar-frontier.com/eng/news/2015/C051171.html, accessed: March 2016.

[17] Roland Scheer, Hans-Werner Schock, *Chalcogenide Photovoltaics Physics, Technologies, and Thin Film Devices*, Wiley-VCH, Weinheim **2011**.

[18] M. Nichterwitz, T. Unold, *J. Appl. Phys.* **2013**, *114*.

[19] R. Scheer, C. Knieper, L. Stolt, *Appl. Phys. Lett.* **1995**, *67*, 3007-3009.

[20] G. Brown, V. Faifer, A. Pudov, S. Anikeev, E. Bykov, M. Contreras, J. Q. Wu, *Appl. Phys. Lett.* **2010**, *96*.

[21] A. E. Grun, *Z Naturforsch Pt A* **1957**, *12*, 89-95.

[22] H. Demers, N. Poirier-Demers, A. R. Couture, D. Joly, M. Guilmain, N. de Jonge, D. Drouin, *Scanning* **2011**, *33*, 135-146.

[23] B. Vermang, J. T. Watjen, C. Frisk, V. Fjallstrom, F. Rostvall, M. Edoff, P. Salome, J. Borme, N. Nicoara, S. Sadewasser, *IEEE J. Photovolt.* **2014**, *4*, 1644-1649.

[24] B. Vermang, J. T. Watjen, V. Fjallstrom, F. Rostvall, M. Edoff, R. Kotipalli, F. Henry, D. Flandre, *Prog. Photovoltaics* **2014**, *22*, 1023-1029.

[25] B. Vermang, V. Fjallstrom, X. D. Gao, M. Edoff, *IEEE J. Photovolt.* **2014**, *4*, 486-492.

[26] F. Pianezzi, S. Nishiwaki, L. Kranz, C. M. Sutter-Fella, P. Reinhard, B. Bissig, H. Hagendorfer, S. Buecheler, A. N. Tiwari, *Prog. Photovoltaics* **2015**, *23*, 892-900.

[27] P. D. Ye, G. D. Wilk, B. Yang, J. Kwo, S. N. G. Chu, S. Nakahara, H. J. L. Gossmann, J. P. Mannaerts, M. Hong, K. K. Ng, J. Bude, *Appl. Phys. Lett.* **2003**, *83*, 180-182.

[28] B. Hoex, S. B. S. Heil, E. Langereis, M. C. M. van de Sanden, W. M. M. Kessels, *Appl. Phys. Lett.* **2006**, *89*.

[29] K. Orgassa, PhD Thesis, University of Stuttgart, May, **2004**.

[30] S. Minoura, K. Kodera, T. Maekawa, K. Miyazaki, S. Niki, H. Fujiwara, *J. Appl. Phys.* **2013**, *113*.

[31] R. Carron, E. Avancini, B. Bissig, P.A. Losio, B. Ruhstaller, J. Steinhauser, S. Buecheler, A. N. Tiwari, Refractive indices of layers of Cu(In,Ga)Se2 solar cells, Lille, 2016).

[32] M. Burgelman, P. Nollet, S. Degrave, *Thin Solid Films* **2000**, *361*, 527-532.

[33] B. Hoex, J. J. H. Gielis, M. C. M. V. de Sanden, W. M. M. Kessels, *J. Appl. Phys.* **2008**, *104*.

[34] B. Shin, J. R. Weber, R. D. Long, P. K. Hurley, C. G. Van de Walle, P. C. McIntyre, *Appl. Phys. Lett.* **2010**, *96*.

[35] J. Joel, B. Vermang, J. Larsen, O. Donzel-Gargand, M. Edoff, *Phys. Status Solidi RRL* **2015**, *9*, 288-292.

[36] W. W. Hsu, J. Y. Chen, T. H. Cheng, S. C. Lu, W. S. Ho, Y. Y. Chen, Y. J. Chien, C. W. Liu, *Appl. Phys. Lett.* **2012**, *100*.

[37] R. Kotipalli, B. Vermang, J. Joel, R. Rajkumar, M. Edoff, D. Flandre, *AIP Adv.* **2015**, *5*.

[38] D. Cahen, R. Noufi, *Appl. Phys. Lett.* **1989**, *54*, 558-560.

[39] U. Rau, D. Braunger, R. Herberholz, H. W. Schock, J. F. Guillemoles, L. Kronik, D. Cahen, *J. Appl. Phys.* **1999**, *86*, 497-505.

[40] L. Kronik, U. Rau, J. F. Guillemoles, D. Braunger, H. W. Schock, D. Cahen, *Thin Solid Films* **2000**, *361*, 353-359.

[41] A. G. Aberle, S. Glunz, W. Warta, *J. Appl. Phys.* **1992**, *71*, 4422-4431.

[42] L. Kranz, C. Gretener, J. Perrenoud, R. Schmitt, F. Pianezzi, F. La Mattina, P. Blosch, E. Cheah, A. Chirila, C. M. Fella, H. Hagendorfer, T. Jager, S. Nishiwaki, A. R. Uhl, S. Buecheler, A. N. Tiwari, *Nat. Commun.* **2013**, *4*.

[43] M. Werner, D. Keller, S. G. Haass, C. Gretener, B. Bissig, P. Fuchs, F. La Mattina, R. Erni, Y. E. Romanyuk, A. N. Tiwari, *ACS Appl. Mater. Interfaces* **2015**, *7*, 12141-12146.

[44] E. Avancini, B. Bissig, P. Reinhard, R. Carron, S. Nishiwaki, T. Feurer, S. Buecheler, A. N. Tiwari, presented at the EMRS Spring Meeting, Lille, 05 May, **2016**.

[45] S. G. Haass, M. Diethelm, M. Werner, B. Bissig, Y. E. Romanyuk, A. N. Tiwari, *Adv. Energy Mater.* **2015**, *5*.

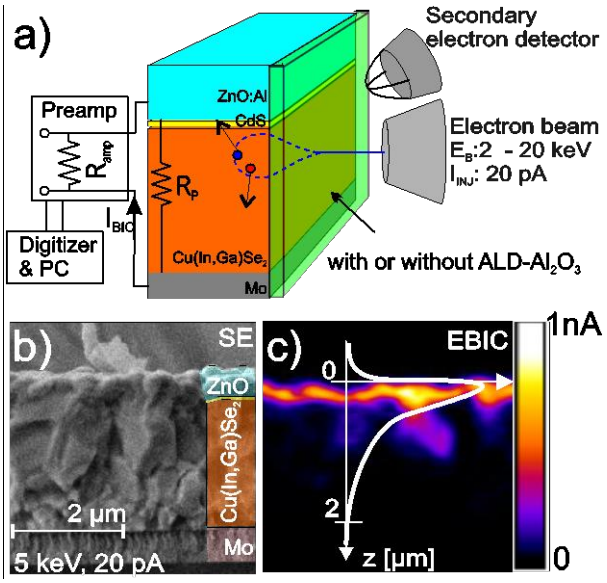

Figure 1: a) Experimental configuration of cross section EBIC measurements: The secondary electron microscope beam scans the sample cross section and the induced current is recorded simultaneously with the secondary electron signal, see b) and c). The inset graph in c) shows a sketch of a typical EBIC profile along the x-direction. No Al_2O_3 coating was applied in the example shown in Figure 1 c).

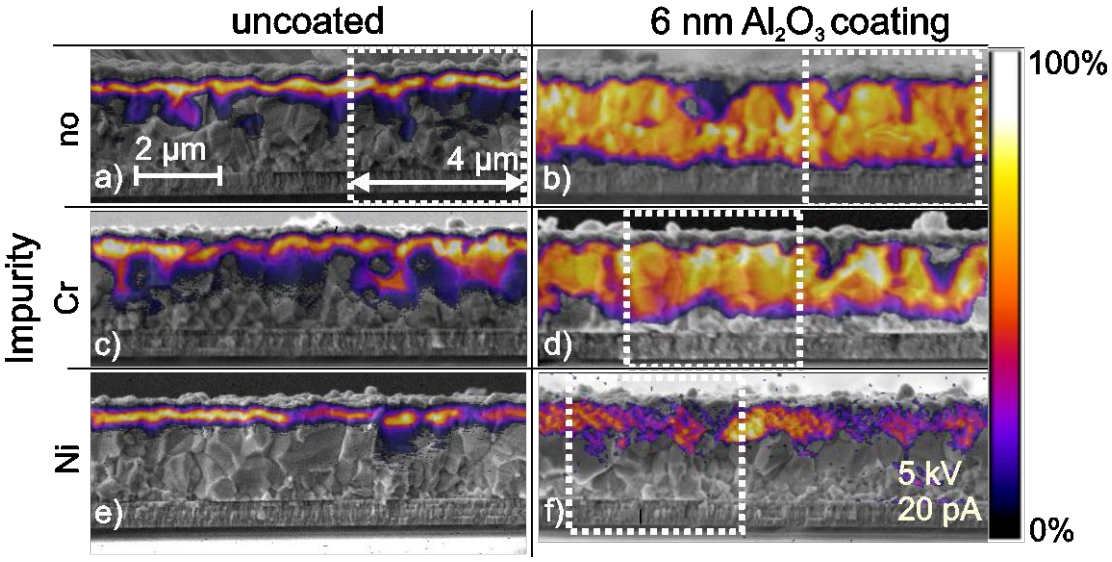

Figure 2: Overlays of SE micrographs and normalized EBIC maps. The left (right) hand side displays measurements on CIGS device cross sections without (with 6nm ALD deposited)

alumina. Top/middle/bottom shows the reference, the Cr and the Ni impurity device. The white boxes indicate representative regions over which horizontal integration was performed for the profiles shown and discussed later. Note that background level was set transparent in the overlay.

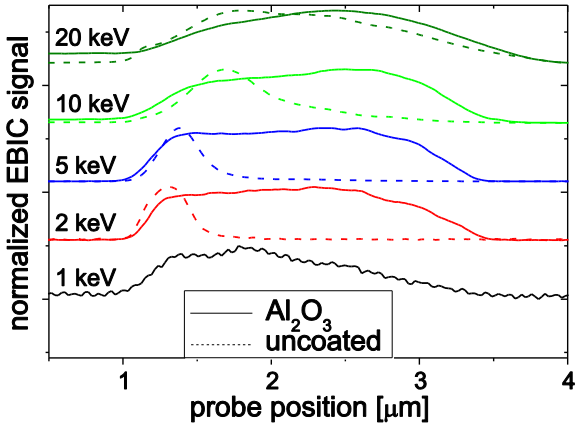

Figure 3: EBIC profiles of the reference sample for increasing beam energy for cases with (solid) and without (dashed) Al_2O_3 coating measured with 20 pA injection current.

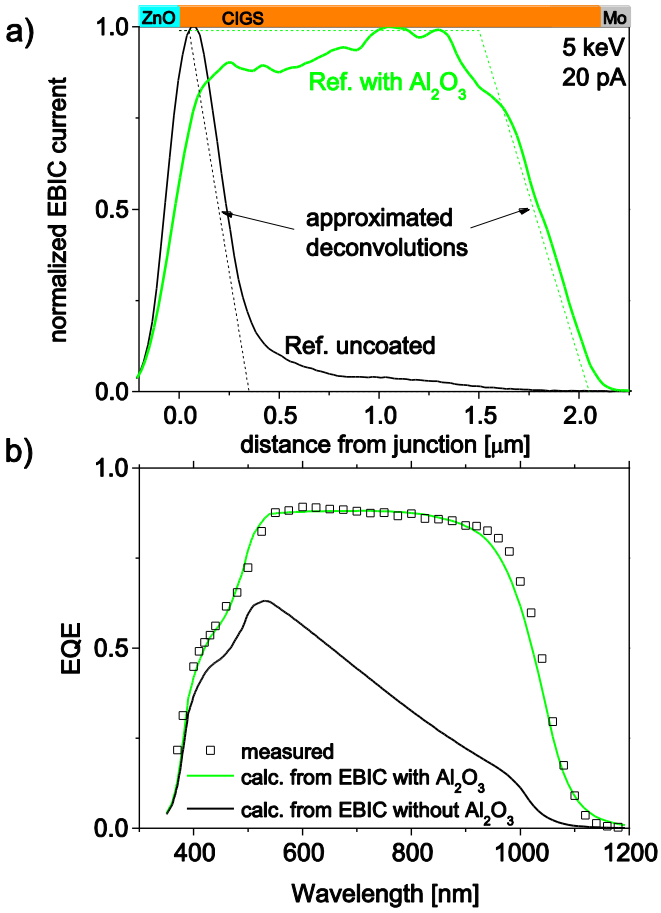

Figure 4 a): The solid lines display normalized EBIC profiles horizontally averaged over the indicated boxes in Figures 2a) and 2b). The dashed lines show numerical approximations as used for the calculation of the EQE. b) Measured (squares) and calculated (lines) external quantum efficiencies (EQE) for the reference sample based on EBIC measurements with (green) and without (black) Al_2O_3 coated cross section.

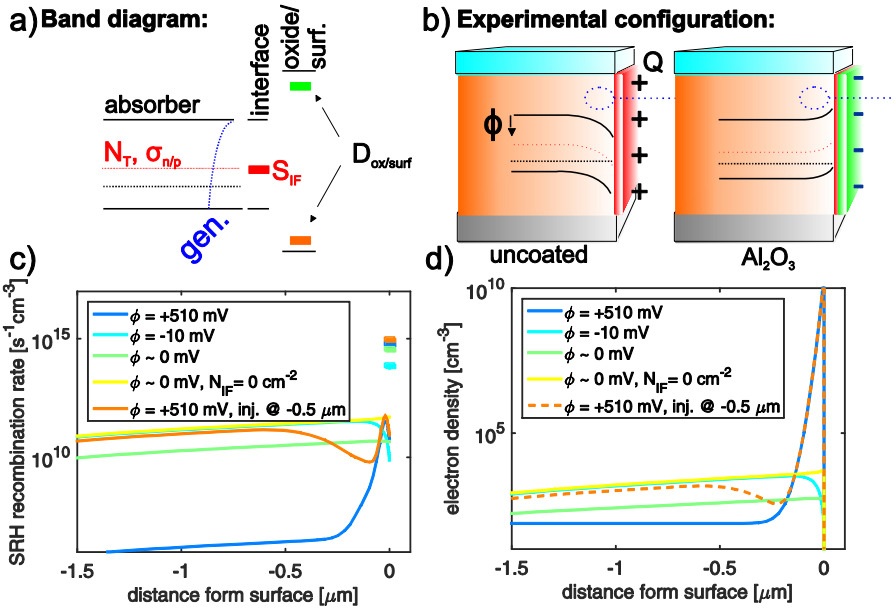

Figure 5: a) Schematics of the SCAPS surface recombination model consisting of the absorber bulk, an interface defect layer and a surface oxide layer. b) Schematics compiling the measurement and model geometry. The model describes a vertical cut through the cross section. c) Steady state Shockley-Read-Hall recombination rates as simulated by SCAPS for different surface band bending under steady state carrier generation by the electron beam. The corresponding steady state electron densities are shown in d).

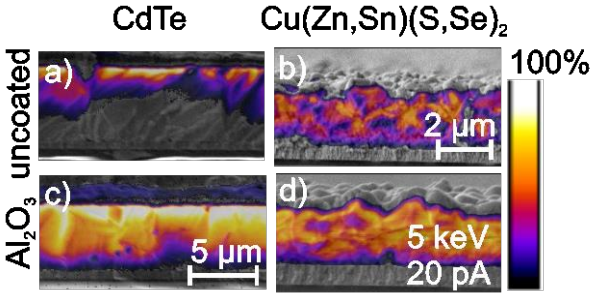

Figure 6: EBIC and SE overlays for CdTe (left) and Kesterite (right) devices without (top) and with (bottom) Al_2O_3 coating. The EBIC signal is extends further and more homogeneous towards the back contact in case of Al_2O_3 coating.

List of Tables:

Table 1: PV parameters for CIGS, CdTe and $Cu_2(Zn,Sn)(S,Se)_4$ devices investigated in this study. In case of CIGS the CGI ([Cu]/([Ga]+[In])) and GGI ([Ga]/([Ga]+[In]) ratios were measured by XRF. For samples with added impurity c_{imp} denotes the concentration of respective impurity as determined by ICPMS.[26] In the case of CdTe c_{imp} denotes the nominally introduced Cu concentration.[42]

Absorber	V_{OC} [mV]	J_{SC} [mA/cm^2]	FF [%]	η [%]	R_P [kΩcm^2]	CGI	GGI	c_{imp} [at%]
CIGS Reference	692	31.2	77.1	16.6	1-10	0.82	0.37	<0.05
CIGS:Cr	592	29.7	65.6	11.5	1-4	0.84	0.37	0.22
CIGS:Ni	351	15.2	48.8	2.6	1-2	0.83	0.38	0.26
CdTe:Cu	840	20.9	69	12.1	~6	-	-	~ 10^{-3}
$Cu_2(Zn,Sn)(S,Se)_4$	442	34.3	58	8.8	4-9	-	-	-